



Probing the limits of optical cycling in a predissociative diatomic molecule

Qi Sun,¹ Claire E. Dickerson ,² Jinyu Dai,¹ Isaac M. Pope,¹ Lan Cheng,³ Daniel Neuhauser,² Anastassia N. Alexandrova,² Debayan Mitra ,^{1,*} and Tanya Zelevinsky¹

¹*Department of Physics, Columbia University, New York, New York 10027-5255, USA*

²*Department of Chemistry and Biochemistry, University of California, Los Angeles, California 90095, USA*

³*Department of Chemistry, The Johns Hopkins University, Baltimore, Maryland 21218, USA*



(Received 5 June 2023; accepted 3 October 2023; published 20 October 2023)

Molecular predissociation, the spontaneous nonradiative bond-breaking process, can limit the ability to scatter a large number of photons required to reach the ultracold regime in laser cooling. Unlike rovibrational branching, predissociation is irreversible since the fragments fly apart with high kinetic energy. Of particular interest is the simple diatomic molecule CaH, for which the two lowest electronically excited states used in laser cooling, $A^2\Pi_{1/2}$ and $B^2\Sigma^+$, lie above the dissociation threshold of the ground potential. In this work, we present measurements and calculations that quantify the predissociation probabilities P_{pd} affecting the cooling cycle. For the lowest vibrational levels, we find P_{pd} of $\sim 10^{-6}$ for $A(v' = 0)$ and $\sim 10^{-3}$ for $B(v' = 0)$. The results allow us to design a laser-cooling scheme that will enable the creation of an ultracold and optically trapped cloud of CaH molecules. In addition, we use the results to propose a two-photon pathway to controlled dissociation of the molecules in order to gain access to their ultracold fragments, including hydrogen.

DOI: [10.1103/PhysRevResearch.5.043070](https://doi.org/10.1103/PhysRevResearch.5.043070)

I. INTRODUCTION

Rapid and repeated photon scattering is not only an efficient method of removing entropy from an atom or a molecule via photon recoils [1], but it also enables the high-fidelity single quantum state preparation and measurement needed for quantum information protocols [2,3]. Optical cycling between the ground state and a low-lying electronic excited state, pioneered with SrF [4] and CaF [5,6], has led to recent progress with laser-cooled molecules such as tweezer arrays of CaF [7], a three-dimensional lattice of YO [8], magneto-optical trapping (MOT) of CaOH [9], and one-dimensional Sisyphus cooling of CaOCH₃ [10].

The primary challenge of direct laser cooling is the large photon budget necessary for bringing a cryogenically pre-cooled molecular beam to within the MOT capture velocity [11,12]. For example, typical molecular beams emanating from a cryogenic buffer gas beam (CBGB) source travel at mean forward velocities of ~ 200 m/s [13]. The recoil velocity per photon is ~ 2 cm/s, hence $>10^4$ photon scatters are needed to bring the molecular beam to a standstill. The photons must be scattered faster than 10^6 s⁻¹ to accomplish slowing within a ~ 1 m distance. Satisfying these criteria can be challenging for molecules with complex internal structures. Indeed, alternative slowing schemes such as traveling wave

Stark deceleration [14], the electro-optic Sisyphus effect [15], centrifuge deceleration [16], and Zeeman-Sisyphus slowing [17] have been demonstrated. These alternative schemes leverage state-dependent electric and magnetic field dependencies to remove entropy with minimal photon scatters. However, quantum-state-resolved detection still requires optical cycling. Although calcium monohydride (CaH) was among the earliest candidates proposed for laser cooling [18], experimental progress was made only recently [19]. One of the reasons is the unique electronic structure of CaH compared to alkaline-earth monohalides [20]. In CaH, the lowest-energy excited state $A^2\Pi_{1/2}(v' = 0)$ lies 556 cm⁻¹ above the Ca(¹S)+H(²S) dissociation threshold of the ground $X^2\Sigma^+$ manifold [Fig. 1(a)], so a molecule in the excited state could decay into the continuum via a radiationless transition. This phenomenon, known as predissociation [21,22], is traditionally studied by observing spectral line shapes and widths inconsistent with radiative decay. A predissociated molecule cannot be repumped into optical cycling because of the significant physical separation and relative velocity of the fragments. Hence the predissociation probability (P_{pd}) sets a limit on the number of photons one can scatter with laser cooling.

Despite the fact that the $A^2\Pi$ state in CaH lies above the ground-state threshold energy, predissociation from $A^2\Pi$ to the $X^2\Sigma^+$ continuum is nominally forbidden due to the von Neumann–Wigner noncrossing rule [23]. For diatomic molecules, states with different symmetries cross while those with the same symmetries form avoided crossings [24,25] (i.e., the molecular Hamiltonian does not couple states with different symmetries). The second-lowest excited $B^2\Sigma^+$ state is allowed to predissociate. However, effects such as spin-orbit coupling can lead to mixing of $A^2\Pi$ and $B^2\Sigma^+$ states,

*dm3710@columbia.edu

Published by the American Physical Society under the terms of the [Creative Commons Attribution 4.0 International license](https://creativecommons.org/licenses/by/4.0/). Further distribution of this work must maintain attribution to the author(s) and the published article's title, journal citation, and DOI.

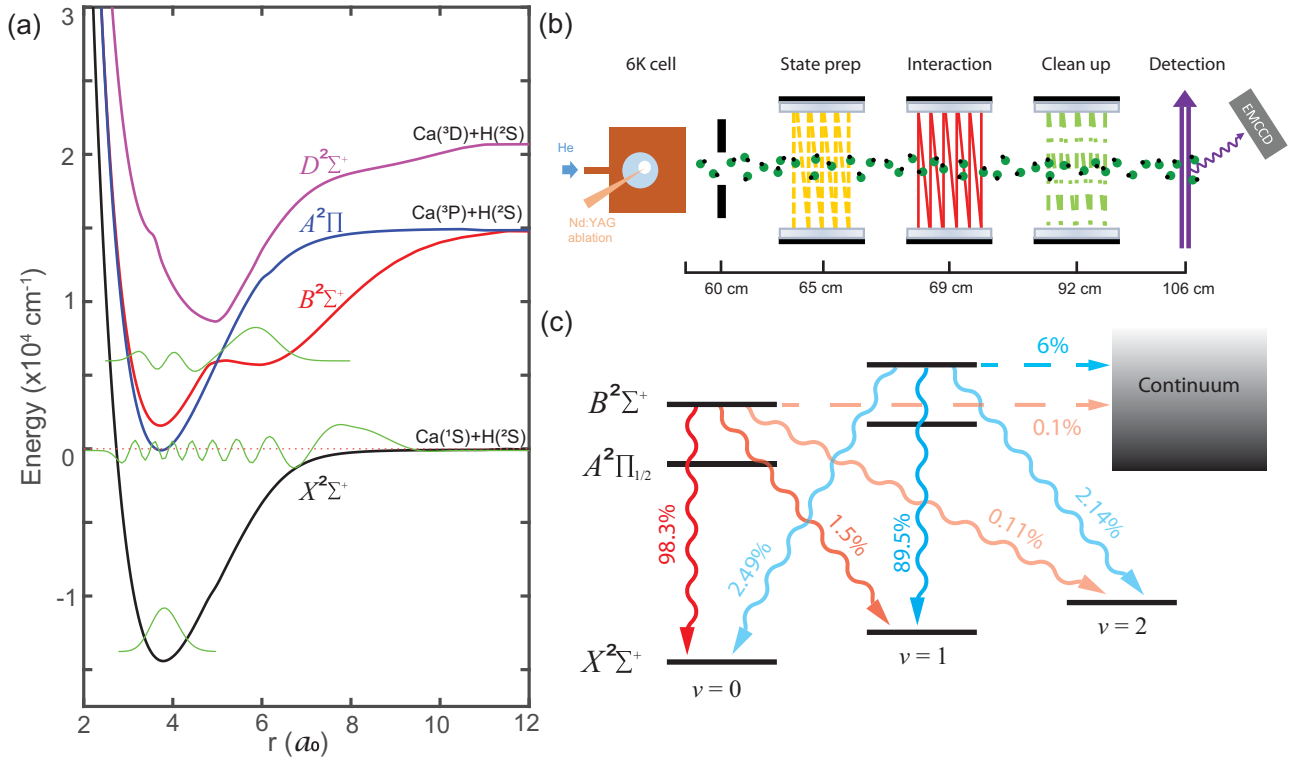


FIG. 1. CaH molecular properties relevant to this work. (a) Potential energy surfaces (PESs) for the four lowest electronic states: $X^2\Sigma^+$, $A^2\Pi$, $B^2\Sigma^+$, and $D^2\Sigma^+$. Spin-orbit interaction is omitted. The x axis is the internuclear separation r in Bohr radii (a_0) and the y axis is energy in cm^{-1} ($1 \text{ cm}^{-1} \approx 30 \text{ GHz}$). The energy origin is chosen as the $\text{Ca}(^1S)+\text{H}(^2S)$ continuum threshold (v_{th}). Superimposed are the wavefunctions (bottom to top) for the $X(v''=0)$ absolute ground state, $X(v''=15)$ least-bound state, and $B(v'=4)$ excited state. (b) Experimental layout used in this work. A buffer-gas-cooled molecular beam emanates from the cryogenic cell and encounters four spatially separated regions: state preparation (S), interaction (I), cleanup (C), and detection (D). Each region includes multipassed lasers described in the text. The diagram is not aligned to scale. (c) Relevant vibrational branching ratios (squiggly arrows) calculated for the $B^2\Sigma^+$ state. The hyperfine structure of the excited states is unresolved. Measured predissociation probabilities for $B(v'=0)$ and $B(v'=1)$ are denoted by dashed lines.

resulting in a small but finite P_{pd} for $A^2\Pi$. Both A and B states are important for efficient optical cycling.

In this work, we present theoretical analysis and measurements of predissociation probability for the $B^2\Sigma^+$ state of CaH. We perform *ab initio* calculations of the potential energy surfaces for CaH, and confirm their accuracy by extracting the Franck-Condon factors (FCFs) for the primary $A^2\Pi_{1/2} \rightarrow X^2\Sigma^+$ and $B^2\Sigma^+ \rightarrow X^2\Sigma^+$ decays and comparing them to our previous measurements. We calculate a nonradiative decay rate, and obtain an estimate of P_{pd} by comparing it to the radiative decay rate. Next, we present an experimental protocol to measure an upper bound of P_{pd} . We find that $P_{pd} \approx 1 \times 10^{-3}$ for the vibrational ground state ($v'=0$) and $P_{pd} \approx 6 \times 10^{-2}$ for the first vibrationally excited state ($v'=1$) of the $B^2\Sigma^+$ manifold. We deduce that the vibrational ground state of the $A^2\Pi_{1/2}$ manifold predissociates with a $\sim 5 \times 10^{-7}$ probability due to spin-orbit mixing with the B state.

The measured values of P_{pd} imply a $\sim 50\%$ predissociative molecule loss after scattering 10^4 photons, suggesting that a MOT of CaH is feasible. We further extract the dipole matrix elements for all transitions connecting the ground $X^2\Sigma^+(v'')$ states to the excited $B^2\Sigma^+(v')$ states. This allows us to predict a viable stimulated Raman adiabatic passage (STIRAP) pathway to controllably dissociate the CaH molecules and

subsequently trap the resulting ultracold hydrogen atoms, which is a prospective goal for molecular laser cooling and cold chemistry research [26].

II. CALCULATION OF MOLECULAR POTENTIAL ENERGIES

The starting point for our calculations is the construction of the potential energy surface (PES) for CaH. All calculations are performed using the MOLPRO program [27–29]. We adopt a basis set and active space as in Ref. [30], where we use cc-pwCVQZ [31] for the Ca atom and aug-cc-pVQZ [32] for the H atom. Calculations are performed in C_{2v} symmetry, which is the nearest Abelian point group to $C_{\infty v}$. Orbitals are generated with a restricted Hartree-Fock (RHF) formalism, then further optimized in a state-averaged complete active space self-consistent field (SA-CASSCF) [33] calculation involving three active electrons and nine active orbitals. For the Σ^+ states, four states are averaged at equal weights in the SA-CASSCF calculation, with (5,2,2,0) closed and (9,4,4,1) occupied orbitals.

For the $A^2\Pi$ state, since only Abelian group symmetries are available, a two-state SA-CASSCF calculation with the same active space is performed in C_{2v} symmetry involving symmetries 2 and 3 of equal weight to represent the $C_{\infty v}$ $A^2\Pi$

TABLE I. The calculated Franck-Condon factors (FCFs) for CaH, compared to experimental FCFs [19]. The experimental FCFs are derived from measured vibrational branching ratios. Note that the active space is optimized for the B state in this work.

Transition	Vibrational quanta (v'')	FCF calculated ($f_{0v''}$)	FCF measured ($f_{0v''}$)
$A \rightarrow X$	0	0.9788	0.9572(43)
	1	0.0205	0.0386(32)
	2	6.8×10^{-4}	$4.2(3.2) \times 10^{-3}$
	3	4.1×10^{-5}	
$B \rightarrow X$	0	0.9789	0.9807(13)
	1	0.0192	0.0173(13)
	2	1.8×10^{-3}	$2.0(0.3) \times 10^{-3}$
	3	1.4×10^{-4}	

state. These wavefunctions are then used in a multireference configuration interaction calculation with Davidson corrections for higher excitations (MRCI+Q) [34–36]. Here, (3,1,1,0) orbitals make up the core, (5,2,2,0) are closed and (9,4,4,1) are occupied. Electron correlation involving double and single excitations is allowed. The spin-orbit interaction-orbit interaction is incorporated at the MRCI level using the Breit-Pauli Hamiltonian [37].

III. CALCULATION OF FRANCK-CONDON FACTORS

Next, we employ the vibrational wavefunctions obtained in Sec. II to calculate the Frank-Condon factors (FCFs) for the CaH transitions of interest. FCFs are calculated using a grid representation of the vibrational wavefunctions. A spline interpolation is fit to the potential energy surfaces calculated in MOLPRO to create the potential energy functions, $V(r)$. The real-space kinetic energy operator is approximated with the Colbert-Miller derivative [38]. Nonadiabatic coupling vectors are computed analytically with the CP-MCSCF program [39] in MOLPRO and fit to a spline interpolation. They are incorporated into the Hamiltonian by directly adding the nonadiabatic coupling to the momentum operator [40]. The Hamiltonian is diagonalized to obtain eigenvalues and eigenvectors. Our calculations converge with a grid spacing (dr) of $0.007a_0$ and a box size of $16.5a_0$. Details are discussed in Appendix E. We compare our calculated FCFs to previous experimental measurements [19] in Table I. We chose the active space which matched $B^2\Sigma^+$ and $X^2\Sigma^+$ state FCFs and vibrational energies in all calculations, since MRCI spin-orbit coupling (SOC) requires the same active space for all involved states. Therefore, the FCFs for $A^2\Pi$ could be improved with varied active space, but a compromise is made to estimate SOC splittings. Despite this compromise, we find the $A^2\Pi_{1/2}$ potential has the correct shape but a slightly incorrect equilibrium bond length. More details are in Appendix E.

IV. $B^2\Sigma^+$ PREDISSOCIATION ESTIMATE

Predissociation probability estimates are computed using an optical absorbing potential with previously predicted scattering cross sections close to experiment [41–43]. An absorbing potential resembling a decaying half parabola of

the form $-iV(r - r_0)^2/w^2$ is added to the $X^2\Sigma^+$ potential energy starting and centered at $r_0 = 8a_0$ with a width $w = 8a_0$ and a depth of $V = 0.2$ a.u. (4.4×10^4 cm $^{-1}$). Results are insensitive to absorber placement as long as it is placed along the potential energy surface's asymptote [43] and has a width larger than the typical de Broglie wavelength [44]. This creates a channeled flux equation which imposes a boundary condition on the wavefunction and eigenvalues attain an imaginary component. Details can be found in Appendix E.

This component, such as the imaginary eigenvalue of $B(v' = 0)$, is directly related to the nonadiabatic coupling between that vibrational wavefunction and the X continuum (where we place the absorber) as the nonradiative transition rate A_{NR} . We estimate the predissociation probability as the ratio of the calculated nonradiative (A_{NR}) and radiative (A_R) decay rates, $A_{NR}/(A_{NR} + A_R)$.

V. $B^2\Sigma^+$ PREDISSOCIATION MEASUREMENT

A. Experimental setup

The experimental setup has been previously described [19]. Briefly, CaH is generated through ablation of a CaH $_2$ target by a pulsed Nd:YAG laser at a ~ 1 Hz rate. CaH is buffer-gas cooled by helium at 6 K and ejected from the cell aperture to form a beam. The molecules are predominantly in the $X^2\Sigma^+(v'' = 0)$ state. The beam of CaH then enters a high-vacuum chamber which is divided into four regions: state preparation, interaction, cleanup, and detection, as shown in Fig. 1(b). In the first three regions, the molecular beam intersects with transverse lasers that address $X \rightarrow A$ or $X \rightarrow B$ transitions. These lasers can be switched on and off by independent optical shutters. The laser beams are multipassed to increase the interaction time with the molecular beam. In the detection region, we apply a single-pass $X \rightarrow A$ or $X \rightarrow B$ light and use an iXon888 electron multiplying charge coupled device (EMCCD) camera and a Hamamatsu R13456 photomultiplier tube to collect the laser-induced fluorescence (LIF) signals for spatially and temporally resolved detection. Every molecule scatters ~ 20 photons in the detection region, which implies that we are not sensitive to the initial spin rotation and hyperfine distribution. All addressed transitions are from the $X^2\Sigma^+(N'' = 1)$ state (N is the rotational quantum number) to $A^2\Pi_{1/2}(J' = 1/2)$ (J is the total angular momentum quantum number) or $B^2\Sigma^+(N' = 0)$ states in order to obtain rotational closure [18]. We use electro-optic modulators (EOMs) to generate sidebands on all lasers to cover all hyperfine states (HFSs) as well as to address spin-rotation manifolds. The transitions used here are first measured experimentally with HFS resolution. Details of the lasers and transition frequencies can be found in Appendix B.

To concisely describe the lasers used in this study we adopt the notation $M_{v'-v''}^R$, which denotes the transitions addressed and the spatial positions of the lasers. M is A or B , representing the electronic state of the excited manifold. R is S , I , C , or D (state preparation, interaction, cleanup, or detection region). In addition, the $F_{Mv'v''}$ notation describes the vibrational branching ratios (VBRs) from either $A^2\Pi_{1/2}$ or $B^2\Sigma^+$ states (represented by M) to $X^2\Sigma^+$ states. For example, F_{B01} is the VBR from $B^2\Sigma^+(v' = 0)$ to $X^2\Sigma^+(v'' = 1)$. We use

TABLE II. Experimental stages for $B(v' = 0)$ state predissociation measurement. In the second column, $M_{v'-v''}^R$ denotes the laser information. M is A or B , representing the electronic excited state. R denotes the region S , I , or C (see text). The third column contains the normalized ground-state populations using unknown variables and calculated VBRs. The five variables n_1 , κ , F_{B0a} , d_A , and d_B represent $X(v'' = 1)$ state natural population, cleanup efficiency of laser B_{1-0}^C , $B(v' = 0)$ state predissociation probability, depletion efficiency of laser A_{0-0}^I , and depletion efficiency of laser B_{0-0}^I . We denote the VBR normalization factors as $\mathcal{F}_{A_0} \equiv \sum_{i \neq 0} F_{A0i}$, $\mathcal{F}_{B_0} \equiv F_{B0a} + \sum_{i \neq 1} F_{B0i}$, and $\mathcal{F}_{B_1} \equiv F_{B0a} + \sum_{i \neq 0} F_{B0i}$. Additional information is in Appendix C.

Purpose	Upstream laser configuration	Downstream normalized $X^2\Sigma^+(v'' = 0)$ state population	Averaged signal ratio
Unperturbed		1	
Cleanup	B_{0-1}^C	$1 + n_1\kappa F_{B00}/\mathcal{F}_{B_0}$	1.05(2)
X-A Cycling	A_{0-0}^I	d_A	0.018(6)
X-A Cycling + Cleanup	$A_{0-0}^I + B_{0-1}^C$	$d_A + [(1 - d_A)F_{A01}/\mathcal{F}_{A_0} + n_1]\kappa F_{B00}/\mathcal{F}_{B_0}$	0.94(2)
X-B Cycling	B_{0-0}^I	d_B	0.086(8)
X-B Cycling + Cleanup	$B_{0-0}^I + B_{0-1}^C$	$d_B + [(1 - d_B)F_{B01}/\mathcal{F}_{B_1} + n_1]\kappa F_{B00}/\mathcal{F}_{B_0}$	0.87(2)

similar notation, F_{B0a} and F_{B1a} , to represent predissociation probabilities from $B^2\Sigma^+(v' = 0)$ and $(v' = 1)$ states.

B. $B^2\Sigma^+(v' = 0)$ predissociation measurement method

To measure the predissociation probability of the $B^2\Sigma^+(v' = 0)$ state, we need to scatter many photons via $B^2\Sigma^+(v' = 0)$ and detect population loss that cannot be explained by known effects, predominantly rovibrational losses. To characterize the loss we design several experimental stages, each stage corresponding to a unique configuration of lasers interacting with the molecular beam. We monitor the population of the $v'' = 0$ ground state in the detection region by detecting LIF signals from the B_{0-0}^D laser. For this measurement we employ six stages. By defining temporally stable parameters that describe the properties of our system, we can express the molecular population distribution at each stage.

For example, in the Unperturbed stage we detect $X(v'' = 0)$ population denoted by N . This is the calibration signal used as a reference. In the Cleanup stage we apply the B_{0-1}^C laser, and the resulting $X(v'' = 0)$ population is $N + n_1N\kappa F_{B00}/\mathcal{F}_{B_0}$ where n_1 is the normalized natural population of $X(v'' = 1)$, κ is the cleanup laser efficiency, and $\mathcal{F}_{B_0} \equiv F_{B0a} + \sum_{i \neq 1} F_{B0i}$ is the VBR normalization factor. This factor accounts for the discrete probability distribution of decay processes based on the VBRs and P_{pd} . By taking the ratio of the integrated signal of the $X(v'' = 0)$ population from the Cleanup stage with signal from the Unperturbed stage, we get the parametrized ratio $R_1 = 1 + n_1\kappa F_{B00}/\mathcal{F}_{B_0}$. In addition to the Unperturbed and Cleanup stages, we have four more stages in this measurement, resulting in a total of five ratios and five parameters (including P_{pd}). The details of all the stages, such as the laser configurations and expressions for the normalized signal, are in Table II and Appendix C. Thus we acquire five equations (measured ratios equal to the parametrized expressions) and five variables. We can solve the equations and express F_{B0a} via R_i s. By precisely measuring R_i we can estimate the $B^2\Sigma^+(v' = 0)$ predissociation probability.

C. $B^2\Sigma^+(v' = 1)$ predissociation measurement method

For the $B(v' = 1)$ state, predissociation is also measured within the framework of stages. We implement two different

methods, each consisting of multiple laser configurations, to measure the same quantity. In method I we use six stages, always monitoring the $X(v'' = 0)$ population downstream using laser A_{0-0}^D . The aim is to populate $X(v'' = 1)$ via an off-diagonal pumping laser A_{1-0}^S and perform optical cycling between $X(v'' = 1)$ and $B(v' = 1)$. We expect to see an increase of the $X(v'' = 0)$ population as a result of the cycling. We repump the molecules remaining in $X(v'' = 1)$ to $v'' = 0$. The recovered population might be less than expected due to vibrational loss. By ruling out other effects, we attribute the loss to $B(v' = 1)$ predissociation. The details of the six stages are in Table III.

Method II differs in several ways. We monitor the $X(v'' = 1)$ population instead of $v'' = 0$, accounting for loss to both $v'' = 0$ and $v'' = 2$ with a sufficient signal-to-noise ratio (SNR) using laser B_{1-1}^D . The ten stages in this method lead to nine measured ratios. And the seven required parameters imply that there are more equations than variables. To find the optimal solution of this overconstrained system, we define a least-squares objective function and use the Levenberg-Marquardt algorithm to search for the local minimum in the parameter space with reasonable initial guesses.

D. Predissociation measurement analysis

The yield of our CBGB source exhibits some slow drift. In order to reduce errors due to molecule number fluctuations, we insert a reference stage before and after every other stage within a group when taking data. For example, in the $B(v' = 0)$ predissociation measurement, data are taken in the following order: *Unperturbed* \rightarrow *Cleanup* \rightarrow *Unperturbed* \rightarrow *X-A Cycling* \rightarrow *Unperturbed* \dots *X-B Cycling + Cleanup* \rightarrow *Unperturbed*. The reference stage for $B(v' = 1)$ method I is Unperturbed, while for method II it is State Prep + Cleanup v0. To calculate the ratios, we divide the signal by the average signal from the calibration shots before and after. The entire group of measurements is repeated multiple times. The averaged ratios can be found in Tables II–IV. The values in parentheses denote the 2σ statistical errors. A graphical representation of the analysis process and histograms of all five ratios can be found in Fig. 2.

With the ratios measured, we use a bootstrap method [45–47] to derive the mean values and build the confidence

TABLE III. Method I of $B^2\Sigma^+(v' = 1)$ predissociation measurement. Notation is similar to Table II. In the third column, the variables include a , n_1 , κ , F_{B1a} , and d_B , representing state preparation (from $X(v'' = 0)$ to $X(v'' = 1)$) efficiency, $X(v'' = 1)$ natural population, cleanup efficiency of laser A_{0-1}^C , $B(v' = 1)$ predissociation probability, and depletion efficiency of laser B_{1-1}^I . The VBR normalization factors are $\mathcal{F}_{A_1} \equiv \sum_{i \neq 1} F_{A0i}$, $\mathcal{F}_{A_2} \equiv \sum_{i \neq 0} F_{A1i}$, and $\mathcal{F}_{B_2} \equiv F_{B1a} + \sum_{i \neq 1} F_{B1i}$. Additional information is in Appendix C.

Purpose	Upstream laser configuration	Downstream normalized $X^2\Sigma^+(v'' = 0)$ state population	Averaged signal ratio
Unperturbed		1	
State Prep	A_{1-0}^S	$1 - a$	0.22(2)
Cleanup	A_{0-1}^C	$1 + n_1\kappa F_{A00}/\mathcal{F}_{A_1}$	1.10(3)
State Prep + Cleanup	$A_{1-0}^S + A_{0-1}^C$	$1 - a + (n_1 + aF_{A11}/\mathcal{F}_{A_2})\kappa F_{A00}/\mathcal{F}_{A_1}$	1.01(3)
State Prep + X-B 1-1 Cycling	$A_{1-0}^S + B_{1-1}^I$	$1 - a + (n_1 + aF_{A11}/\mathcal{F}_{A_2})d_B F_{B10}/\mathcal{F}_{B_2}$	0.39(2)
State Prep + X-B 1-1 Cycling + Cleanup	$A_{1-0}^S + B_{1-1}^I + A_{0-1}^C$	$1 - a + (n_1 + aF_{A11}/\mathcal{F}_{A_2})(d_B F_{B10}/\mathcal{F}_{B_2} + (1 - d_B)\kappa F_{A00}/\mathcal{F}_{A_1})$	0.40(2)

intervals of the predissociation probabilities depicted in Fig. 3. This method is particularly useful as it does not require any assumptions about the data such as independence assumptions typically made for standard error calculations. We consider several other analysis methods, such as pairwise bootstrapping and regular error propagation, and the outcomes are all in agreement with each other. Details of the bootstrap method are in Appendix D.

After considering all systematic effects and analyzing statistical errors, we find the predissociation probability for the $B^2\Sigma^+(v' = 0)$ state to be $0.00097^{+0.00059}_{-0.00057}$ and for the $B^2\Sigma^+(v' = 1)$ state to be $0.056^{+0.044}_{-0.034}$. The reported value for $B(v' = 1)$ is the average of the two methods (method I yields $0.079^{+0.021}_{-0.017}$ and method II yields $0.033^{+0.013}_{-0.011}$), and the 95% confidence interval is the largest of the two methods combined. These values are consistent with the probabilities calculated in Sec. IV within the order of magnitude. Other potential loss channels are discussed in Appendix A. In addition, to demonstrate the robustness of our measurements to small variations in FCFs, we perform a comparative analysis by utilizing the FCFs obtained in previous theoretical work on CaH [20,48]. The results consistently produce nonzero predissociation probabilities and are within error bars of each

other. The sharp monotonic increase in P_{pd} seen in Fig. 3 can be understood as a bound molecule quantum tunneling through the $B^2\Sigma^+$ potential into the $X^2\Sigma^+$ continuum at the same energy. As the energy of the incident quantum state increases, so does the transmission probability, which is aided by stronger wavefunction overlaps.

VI. $A^2\Pi_{1/2}$ PREDISSOCIATION ESTIMATE

The $A^2\Pi$ state in CaH does not undergo predissociation via the process described for the $B^2\Sigma^+$ state. However, spin-orbit coupling can induce mixing between the A and B states, leading to nonvanishing predissociation of the $A^2\Pi_{1/2}$ spin-orbit state. For a linear molecule, the z component of total angular momentum, J_z , is a good quantum number. Therefore the spin-orbit component $A^2\Pi_{1/2}$ can interact with $B^2\Sigma^+(J_z = 1/2)$ due to the same J_z value. A similar interaction exists between $A^2\Pi_{1/2}$ and $X^2\Sigma^+(J_z = 1/2)$ but the energy separation is much larger ($\sim 14\,000\text{ cm}^{-1}$) compared to that between the A and B states ($\sim 1400\text{ cm}^{-1}$). Higher vibrational states of the X manifold are closer in energy to A but the effective coupling to the states relevant for laser cooling is weaker due to a poor vibrational wavefunction overlap.

TABLE IV. Method II of $B^2\Sigma^+(v' = 1)$ predissociation measurement. In the third column, the seven variables include a , n_1 , κ_1 , κ_2 , F_{B1a} , d_A , and d_B , representing state preparation (from $X(v'' = 0)$ to $X(v'' = 1)$) efficiency, $X(v'' = 1)$ natural population, cleanup efficiency of laser A_{1-0}^C , cleanup efficiency of laser A_{1-2}^C , $B(v' = 1)$ predissociation probability, depletion efficiency of laser A_{1-1}^I , and depletion efficiency of laser B_{1-1}^I . The VBR normalization factors are $\mathcal{F}_{A_2} \equiv \sum_{i \neq 0} F_{A1i}$, $\mathcal{F}_{A_3} \equiv \sum_{i \neq 1} F_{A1i}$, $\mathcal{F}_{A_4} \equiv \sum_{i \neq 2} F_{A1i}$, and $\mathcal{F}_{B_2} \equiv F_{B1a} + \sum_{i \neq 1} F_{B1i}$. Additional information is in Appendix C.

Purpose	Upstream laser configuration	Downstream normalized $X^2\Sigma^+(v'' = 1)$ state populations	Average ratio
State Prep + Cleanup v0	$A_{1-0}^S + A_{1-0}^C$	$n_1 + (a + \kappa_1 - a\kappa_1)F_{A11}/\mathcal{F}_{A_2}$	
Unperturbed		n_1	0.13(3)
State Prep	A_{1-0}^S	$n_1 + aF_{A11}/\mathcal{F}_{A_2} \equiv \mathcal{Z}$	0.89(4)
Cleanup v0	A_{1-0}^C	$n_1 + \kappa_1 F_{A11}/\mathcal{F}_{A_2}$	0.93(4)
State Prep + X-A 1-1 Cycling	$A_{1-0}^S + A_{1-1}^I$	$\mathcal{Z}(1 - d_A)$	0.03(3)
State Prep + X-A 1-1 Cycling + Cleanup v0	$A_{1-0}^S + A_{1-1}^I + A_{1-0}^C$	$\mathcal{Z}(1 - d_A) + (1 - a + \mathcal{Z}d_A F_{A10}/\mathcal{F}_{A_3})\kappa_1 F_{A11}/\mathcal{F}_{A_2}$	0.33(3)
State Prep + X-A 1-1 Cycling + Cleanup v2	$A_{1-0}^S + A_{1-1}^I + A_{1-2}^C$	$\mathcal{Z}(1 - d_A) + (aF_{A12}/\mathcal{F}_{A_2} + \mathcal{Z}d_A F_{A12}/\mathcal{F}_{A_3})\kappa_2 F_{A11}/\mathcal{F}_{A_4}$	0.57(4)
State Prep + X-B 1-1 Cycling	$A_{1-0}^S + B_{1-1}^I$	$\mathcal{Z}(1 - d_B)$	0.12(3)
State Prep + X-B 1-1 Cycling + Cleanup v0	$A_{1-0}^S + B_{1-1}^I + A_{1-0}^C$	$\mathcal{Z}(1 - d_B) + (1 - a + \mathcal{Z}d_B F_{B10}/\mathcal{F}_{B_2})\kappa_1 F_{A11}/\mathcal{F}_{A_2}$	0.35(3)
State Prep + X-B 1-1 Cycling + Cleanup v2	$A_{1-0}^S + B_{1-1}^I + A_{1-2}^C$	$\mathcal{Z}(1 - d_B) + (aF_{A12}/\mathcal{F}_{A_2} + \mathcal{Z}d_B F_{B12}/\mathcal{F}_{B_2})\kappa_2 F_{A11}/\mathcal{F}_{A_4}$	0.42(3)

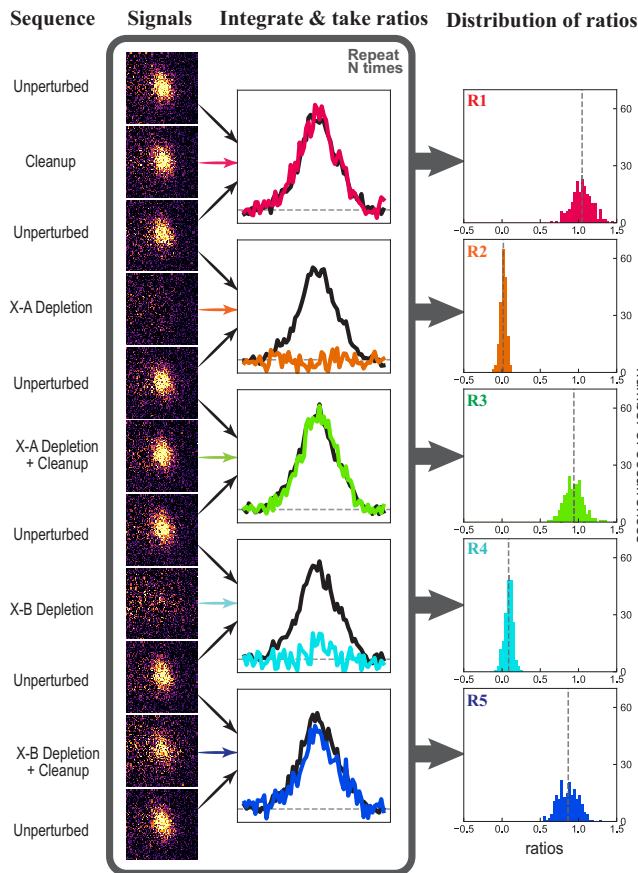


FIG. 2. Illustration of the ratio extraction process for the $B^2\Sigma^+(v' = 0)$ predissociation measurement. We run the stages sequentially with an interlaced reference stage, and collect LIF with an EMCCD. We integrate the images along both axes to obtain the signals, which we then use to calculate ratios. By repeating the entire sequence N times, we collect N sets of five ratios. Here we first show examples of one-shot camera images. We then present the integrated signal along one axis, using colored traces for science stages and black for reference stages (horizontal lines are the baselines). Finally we show the histograms of the five ratios. The widths of the histograms are a combination of source fluctuations and detection noise due to the EMCCD camera, which can be independently calibrated. Vertical dashed lines represent the means of the ratios.

We estimate the mixing between the $A(v' = 0)$ and the $B(v' = 0)$ states separated by 1400 cm^{-1} . The spin-orbit parameters are obtained with the Breit-Pauli Hamiltonian at the MRCI level [37] and are given in Table V. Diagonalization of this Hamiltonian matrix leads to a 0.05% $B(v' = 0)$ admixture into the $A(v' = 0)$ state. Similarly, we can compute the mixing between $A(v' = 1)$, $B(v' = 0)$, and $B(v' = 1)$. The coupling between $A(v' = 1)$ and $B(v' = 1)$ is expected to be similar to the case of $v' = 0$ since the energy difference of 1310 cm^{-1} is similar to that in the case of $v' = 0$. However, the $A(v' = 1)$ and $B(v' = 0)$ states are only 64 cm^{-1} apart, hence even a small FCF can lead to significant mixing. Note that the measured FCF for the $A(v' = 0) \rightarrow X(v'' = 1)$ transition is 4% (Table I) and that our calculated A - B bond length difference is smaller than the X - A bond length. We use $f = 5\%$ as an upper limit for the $A(v' = 1) \rightarrow B(v' = 0)$ FCF. Diagonal-

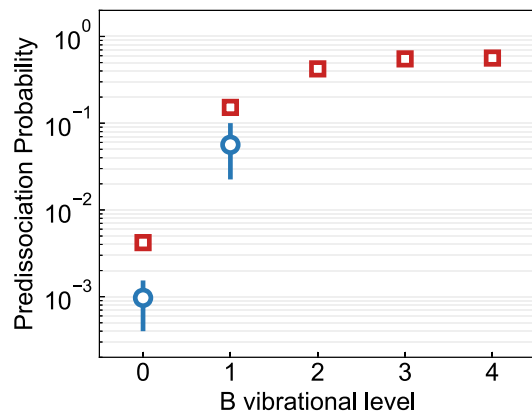


FIG. 3. CaH predissociation. Red squares are theoretical results for nonradiative decay rates of different vibrational states of $B^2\Sigma^+$. Blue circles are experimental results, where error bars represent the 95% confidence interval.

ization of the corresponding Hamiltonian matrix in Table V yields an 8.4% $B(v' = 0)$ character for $A(v' = 1)$. Combining these admixtures with the measured P_{pd} for $B(v' = 0, 1)$, we estimate that the $A(v' = 0)$ state very weakly predissociates with a probability of $\sim 5 \times 10^{-7}$ and the $A(v' = 1)$ state with a higher probability of $\sim 3 \times 10^{-5}$. The FCF used here is an upper-bound value and therefore the estimated probabilities serve as upper bounds.

VII. CONTROLLED DISSOCIATION PATHWAY

As mentioned in Sec. I, an enticing application of ultracold CaH and other molecules is controlled dissociation into fragments that are not directly laser coolable, such as H. In order to trap the resulting H atoms, their maximum kinetic energy must be below typical optical trap depths. A magic-wavelength trap for H atoms at 513 nm has a depth of 1.2 kHz per 10 kW/cm^2 [49]. A practical dipole trap with an intensity of at most $\sim 100\text{ kW/cm}^2$ would result in a maximum trap depth of only $\sim 0.5\text{ }\mu\text{K}$. Since the binding energy of $B^2\Sigma^+(v' = 0)$ corresponds to a temperature of $\sim 1000\text{ K}$, the trapping of the fragments relies on the ability to dissociate the molecules as closely as possible to the threshold [26], such as via a stimulated two-photon process [50,51].

Stimulated Raman adiabatic passage (STIRAP) is a technique that has been successfully employed to generate ground-state bialkali molecules starting from a weakly bound state [52,53]. Although STIRAP has been predominantly demonstrated for adiabatic population transfers from weakly bound to deeply bound molecular states, the mechanism can be extended to unbound continuum states [54,55]. A prerequisite for efficient transfer is the identification of an intermediate state that strongly couples to both initial and final states. Additionally, a desirable intermediate state would be connected via readily accessible laser wavelengths to the initial and final states.

Molecular structure calculations give us access to branching ratios and line strengths for a multitude of vibrational levels, some of which have advantages for controlled dissociation. We calculate the dipole transition line

TABLE V. Spin-orbit matrices accounting for vibrational mixing of the A and B states. The Π_x and Π_y basis states split under SOC to produce $\Pi_{1/2}$ and $\Pi_{3/2}$ states. The top matrix is for $A^2\Pi(v' = 0)$ and $B^2\Sigma^+(v' = 0)$, while the bottom one is for $A^2\Pi(v' = 1)$, $B^2\Sigma^+(v' = 1)$, and $B^2\Sigma^+(v' = 0)$. The Franck-Condon factor f is introduced to account for the off-diagonal vibrational wavefunction overlap. The diagonal terms represent the energies of unperturbed states. All values are in cm^{-1} .

	$A^2\Pi_x$ ($v = 0, m_s = 1/2$)	$A^2\Pi_y$ ($v = 0, m_s = 1/2$)	$B^2\Sigma^+$ ($v = 0, m_s = -1/2$)	
$A^2\Pi_x(v = 0, m_s = 1/2)$	0	$-35.5i$	21.5	
$A^2\Pi_y(v = 0, m_s = 1/2)$	$35.5i$	0	$-21.5i$	
$B^2\Sigma^+(v = 0, m_s = -1/2)$	21.5	$21.5i$	1400	
	$A^2\Pi_x$ ($v = 1, m_s = -1/2$)	$A^2\Pi_y$ ($v = 1, m_s = 1/2$)	$B^2\Sigma^+$ ($v = 0, m_s = -1/2$)	$B^2\Sigma^+$ ($v = 1, m_s = -1/2$)
$A^2\Pi_y(v = 1, m_s = 1/2)$	0	$-35.5i$	$21.5f$	21.5
$A^2\Pi_x(v = 1, m_s = 1/2)$	$35.5i$	0	$-(21.5f)i$	$-21.5i$
$B^2\Sigma^+(v = 0, m_s = -1/2)$	$21.5f$	$(21.5f)i$	64	0
$B^2\Sigma^+(v = 1, m_s = -1/2)$	21.5	$21.5i$	0	1310

strength $S_{v'v''}$, which is the square of the transition dipole moment ($|\langle v' | \mu | v'' \rangle|^2$), for both $A^2\Pi_{1/2} \rightarrow X^2\Sigma^+$ and $B^2\Sigma^+ \rightarrow X^2\Sigma^+$ transitions [Figs. 4(a) and 4(b)]. The PESs for A and X states are similar in shape [Fig. 1(a)], which leads to highly diagonal transition strengths. However, the second minimum in the B -state PES leads to strong off-diagonal coupling starting around $v' = 4$. This feature enables strong coupling of $B(v' = 4)$ to both $X(v'' = 0)$ and $X(v'' = 15)$

[Fig. 4(c)]. Our calculations do not show a significant coupling between the $B(v' = 4)$ state and the vibrationally excited states of the A manifold. Here we calculate the coupling to the weakest bound state, rather than to the continuum, for two reasons. First, we expect the coupling to the lowest-energy continuum states and to the least-bound state to be similar since their energy difference is only $\sim 500 \text{ cm}^{-1}$. Second, we expect the STIRAP process to be more efficient if all three

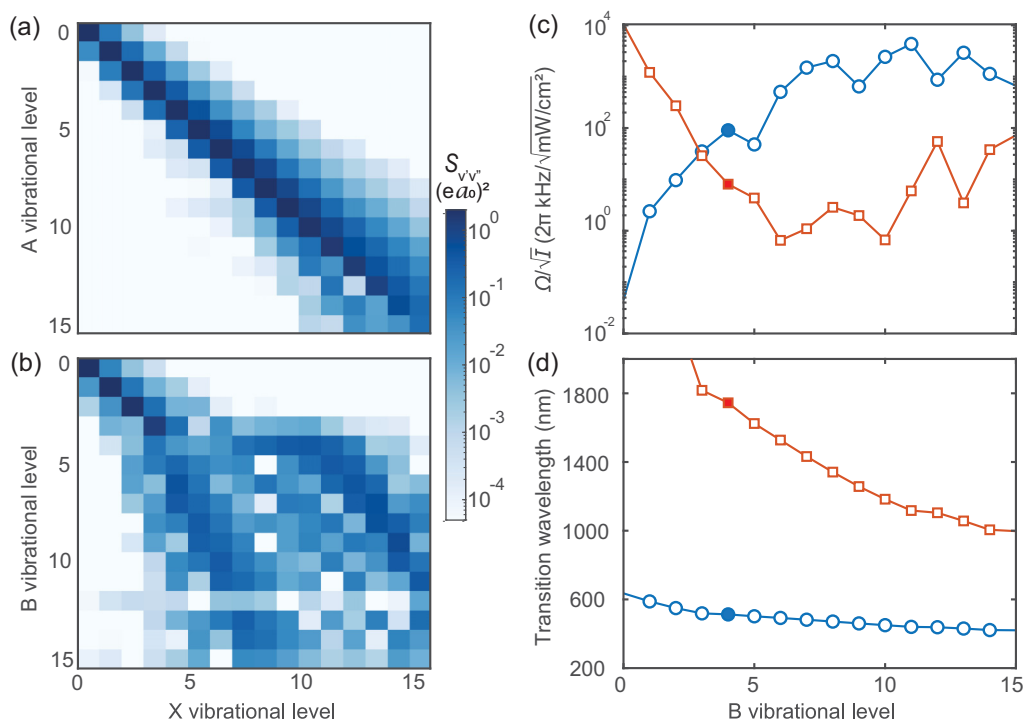


FIG. 4. Suggested controlled dissociation pathway for CaH molecules. Line strengths ($S_{v'v''}$) in atomic units for dipole-allowed transitions: (a) $X^2\Sigma^+(v'') \rightarrow A^2\Pi_{1/2}(v')$ and (b) $X^2\Sigma^+(v'') \rightarrow B^2\Sigma^+(v')$. The A -state potential is more harmonic as is reflected by the diagonal $S_{v'v''}$. The B state, however, significantly deviates from the diagonal starting around $v' = 4$ because of the second potential minimum at $\sim 6a_0$ [Fig. 1(a)]. Note that $B(v' = 4)$ has comparable line strengths between $X(v'' = 0)$ and $X(v'' = 15)$. (c) Intensity-normalized Rabi rate ($\Omega/\sqrt{I} = \sqrt{S_{v'v''}}/\hbar$) for dipole transitions $X(v'' = 0) \rightarrow B(v')$ (red squares) and $B(v') \rightarrow X(v'' = 15)$ (blue circles). Around $v' = 4$ (shaded points), the Rabi rates are comparable. (d) Wavelengths in nanometers for optical transitions $X(v'' = 0) \rightarrow B(v')$ (blue circles) and $B(v') \rightarrow X(\text{continuum})$ (red squares). The theoretical energy differences are adjusted by a common offset of 240 cm^{-1} to match experimental data for $X(v'' = 0) \rightarrow B(v' = 0, 1, 2)$ transitions [57]. The wavelengths corresponding to $v' = 4$ (shaded points) are 512.7 and 1744.7 nm.

TABLE VI. Theoretical and experimental values of predissociation probability for $B^2\Sigma^+$ and $A^2\Pi_{1/2}$. Both radiative (A_R) and nonradiative (A_{NR}) decay rates are calculated. The radiative lifetime is $\tau \equiv 1/A_R$. Predissociation P_{pd} probability is defined as the ratio of the nonradiative decay rate to the total decay rate ($A_R + A_{NR}$). Measurements of P_{pd} are only provided for the $B^2\Sigma^+(v' = 0)$ and ($v' = 1$) states. For the latter, we report the mean of two different measurement methods described in Sec. VC. The values given for the $A^2\Pi_{1/2}(v' = 0)$ and ($v' = 1$) states are estimated by calculating the spin-orbit mixing between A and B as described in Sec. VI.

State	Vibrational quantum (v'')	Radiative lifetime (ns)	Radiative decay rate (A_R, s^{-1})	Nonradiative decay rate (A_{NR}, s^{-1})	Predissociation (PD) probability	Experimental PD probability
B	0	52.0	1.924×10^7	8.040×10^4	0.0042	$0.00097^{+0.00059}_{-0.00057}$
	1	54.3	1.842×10^7	3.304×10^6	0.1521	$0.056^{+0.044}_{-0.034}$
	2	58.9	1.698×10^7	1.245×10^7	0.4230	
	3	78.2	1.278×10^7	1.571×10^7	0.5514	
	4	59.2	1.688×10^7	2.181×10^7	0.5637	
	5	83.9	1.193×10^7	5.482×10^7	0.8213	
	6	84.4	1.185×10^7	5.960×10^7	0.8342	
A	0	34.3	2.913×10^7			5×10^{-7}
	1	34.5	2.902×10^7			3×10^{-5}

states are bound states. Hence it is worthwhile to consider a transfer to $X(v'' = 15)$ followed by photodissociation [51] or Feshbach dissociation [56].

In Fig. 4(d) we plot the laser wavelengths required to connect $X(v'' = 0)$ as well as the ground-state continuum to the B manifold. We estimate that the “upleg” STIRAP wavelength for $X(v'' = 0) \rightarrow B(v' = 4)$ is 512.7 nm while the “downleg” wavelength for $B(v' = 4) \rightarrow X(v'' = v_{th})$ is 1744.7 nm. Both these wavelengths are accessible via current technology such as Raman fiber amplifiers and difference-frequency generation (DFG). Thus we expect high-power and narrow-linewidth laser sources to be within reach for STIRAP.

VIII. CONCLUSION

Predissociation is a challenge for laser cooling of new molecular species. We have theoretically and experimentally studied it for laser-cooling CaH as well as in the context of controlled ultracold dissociation. We find that the lowest-excited electronic state $A^2\Pi_{1/2}(v' = 0)$, which is the workhorse for optical cycling, only weakly predissociates ($P_{pd} \approx 10^{-6}$) via spin-orbit coupling. The next excited manifold $B^2\Sigma^+$, crucial for repumping vibrational dark states, has much stronger predissociation by virtue of having the same symmetry as $X^2\Sigma^+$. We measure P_{pd} for $B(v' = 0)$ and $B(v' = 1)$ states and obtain $\sim 10^{-3}$ and $\sim 6 \times 10^{-2}$, respectively. This sharp increase is substantiated by theoretical calculations, and we expect $P_{pd} \rightarrow 1$ for $v' \gtrsim 4$. The results are summarized in Table VI.

To obtain high photon scattering rates, one must repump the $A(v' = 0) \rightarrow X(v'' = 1)$ vibrational loss channel via the $B(v' = 0)$ state. Due to predissociation, we find that the optimal laser-cooling scheme requires avoiding the $B(v' \geq 1)$ states in favor of using the A manifold. On average, every cycling molecule will scatter ~ 20 photons [$1/(1 - F_{A00})$] before being lost to $X(v'' = 1)$. Each of these molecules only needs to scatter one photon via $B(v' = 0)$ to return to cycling, but it will predissociate with a 0.1% probability. Hence we estimate that $\sim 50\%$ of molecules will be lost to predissociation after scattering the requisite $\sim 10^4$ photons.

Last, we propose to take advantage of the high predissociation probability for the $B(v' = 4)$ state to engineer a two-photon STIRAP pathway for transferring the molecular population from the ground $X(v'' = 0)$ state to the low-energy continuum $X(v'' = v_{th})$. We find that $B(v' = 4)$ couples strongly to both these X states via optical transitions at wavelengths within accessible laser technologies.

ACKNOWLEDGMENTS

We thank Ian Lane for fruitful discussions of dissociation and Roi Baer for discussions of nonadiabatic couplings. We thank Ye Tian for his assistance in implementing the bootstrapping method used in this study. This work was supported by the ONR Grant No. N00014-21-1-2644, AFOSR MURI Grant No. FA9550-21-1-0069, and we acknowledge generous support by the W. M. Keck Foundation and the Brown Science Foundation. D.N. would like to acknowledge support from the BSF Grant No. 2018368 and NSF-CHE Grant No. 1763176. A.N.A. acknowledges support from the NSF Center for Chemical Innovation Phase I Grant No. CHE-2221453. C.E.D. acknowledges support from NSF Grant No. DGE-2034835.

APPENDIX A: OTHER POSSIBLE LOSS CHANNELS AND THEIR CONTRIBUTIONS

Other potential loss channels that disrupt optical cycling could lead to overestimating the predissociation probability. The theoretical results are agnostic to such processes. We consider the following processes that may contribute to population loss:

(i) Off-resonant excitation to the $B^2\Sigma^+(v' = 0, N' = 2)$ state. The nearest parity-allowed transition from $X(v'' = 0, N'' = 1)$ is to $B(v' = 0, N' = 2)$ which is 768 GHz away from $B(v' = 0, N' = 1)$. The transition linewidth is $\sim 2\pi \times 3$ MHz. Assuming a two-level-like system, the scattering rate is [1]

$$R_{sc} = \frac{s\Gamma/2}{1 + s + (2\Delta/\Gamma)^2}.$$

In our system, the saturation parameter is $s \lesssim 1000$, and thus $R_{sc} \lesssim 2 \text{ s}^{-1}$. This rate is low compared to the estimated nonradiative decay rate of 10^5 s^{-1} ; therefore, off-resonant excitation should not affect the result.

(ii) External electric fields ϵ can induce mixing between $B^2\Sigma^+(v'=0, N'=0)$ and $N'=1$ states (e.g., Ref. [58], Sec. 8.4.2.1). For the $A^2\Pi_{1/2}$ state, the matrix element of the dipole operator $T_p^1(d)$ in Hund's case a basis is $-\frac{1}{3}\epsilon d$. For the $B^2\Sigma^+$ state expressed in Hund's case b basis, we first project to Hund's case a basis, then calculate the matrix element to be $-\frac{1}{2}\epsilon d$. The rotational spacing for $B^2\Sigma^+$ is 250 GHz, while the Λ doubling for $A^2\Pi_{1/2}$ is 26 GHz [57]. The effective decay rate is given by

$$\frac{1}{\tau_{N=0,2}} = R_{sc} \frac{(d\epsilon/2)^2}{4\omega^2 + \Gamma^2/4},$$

where for the A and B states, respectively, the values are $d = 2.57 \text{ D}$ and 3.1 D , $\omega = 2\pi \times 13 \text{ GHz}$ and $2\pi \times 125 \text{ GHz}$, and $\Gamma = 2\pi \times 5 \text{ MHz}$ and $2\pi \times 3 \text{ MHz}$. We assume $R_{sc} \approx 1 \text{ MHz}$. Since we electrically ground the entire vacuum chamber, the electric field amplitude inside the chamber should be $<100 \text{ V/m}$. We find that the possible remixing rate is $6.2 \times 10^{-4} \text{ s}^{-1}$ for $A^2\Pi_{1/2}$ and $9.7 \times 10^{-6} \text{ s}^{-1}$ for $B^2\Sigma^+$. These numbers are several orders of magnitude smaller than nonradiative decay rates and should have a negligible effect.

(iii) Photon scattering along the molecular beam can cause acceleration or deceleration and affect signal strength. In the interaction region we scatter <100 photons per molecule. The laser beams are reflected in a zigzag pattern; i.e., the incidence is not perfectly perpendicular and there is a projection on the beam propagation direction. The angle is estimated to be $\arctan(1/15) \approx 4^\circ$. Hence less than 10 photons worth of momentum is added to the molecular beam, and that would only yield a 15 cm/s velocity change. The beam velocity is $\sim 200 \text{ m/s}$, implying that the effect on the signal is at the 8×10^{-4} level, which is negligible.

(iv) We consider off-diagonal vibrational loss due to spin-orbit mixing. As discussed in Sec. VI, the $B^2\Sigma^+(v'=0)$ state mixes with the $A^2\Pi_{1/2}(v'=1)$ state at the 0.06% level. This implies that population from $B(v'=0)$ can decay to $X(v''=1)$ via $A(v'=1)$ at a rate of $6 \times 10^{-4} \times F_{A10} \approx 5 \times 10^{-4}$. This value is 40 times smaller than the FCF for the $B(v'=0) \rightarrow X(v''=1)$ decay (1.92×10^{-2}) and hence is a negligible correction to our model. A similar argument holds for off-diagonal vibrational loss induced by spin-orbit mixing of the $B(v'=1)$ state with either $A(v'=0)$ or $A(v'=2)$.

APPENDIX B: LASER PARAMETERS AND SPECTROSCOPY OF TRANSITIONS USED IN THIS WORK

Here we describe the lasers used in the experiment, and the transition frequencies. All laser beams pass through an electro-optic modulator (EOM) to generate the sidebands needed to address HFSs.

(a) In the state-preparation region, the A_{1-0}^S light (637 nm) is generated from two sets of injection-locked amplifiers (ILAs) to address the spin-rotation states, with 95 mW of power.

TABLE VII. Frequencies of all transitions used in the experiment. The $A^2\Pi_{1/2}$ and $B^2\Sigma^+$ states have unresolved hyperfine splittings. The uncertainties are 10 MHz statistical and 60 MHz systematic due to the wavemeter.

Ground	v''	N''	J''	F''	Excited	v'	N'	J'	Frequency (THz)
			3/2	2					431.274552
X	0	1	1/2	1	A	0		1/2	431.274653
				0					431.276565
			3/2	2					431.276512
				1					472.026689
X	0	1	1/2	1	B	0	0	1/2	472.026790
				1					472.028702
				0					472.028649
			3/2	2					432.342011
X	1	1	1/2	1	A	1		1/2	432.342120
				0					432.343958
			3/2	2					432.343902
				1					471.557078
X	1	1	1/2	1	B	1	0	1/2	471.557178
				0					471.559025
			3/2	2					471.558969
				1					470.113870
X	0	1	1/2	1	A	1		1/2	470.113971
				0					470.115873
			3/2	2					470.115819
				1					395.717108
X	2	1	1/2	1	A	1		1/2	395.717218
				0					395.718978
			3/2	2					395.718928
				1					434.254840
X	1	1	1/2	1	B	0	0	1/2	434.254949
				0					434.256787
			3/2	2					434.256731
				1					393.502723
X	1	1	1/2	1	A	0		1/2	393.502832
				0					393.504670
				0					393.504614

(b) In the interaction region, multiple lasers are applied. A_{0-0}^I (695 nm) or A_{1-1}^I (693 nm) light is derived from two ILAs that provide 60 mW in total. B_{0-0}^I (635 nm) or B_{1-1}^I (636 nm) is from two external-cavity diode lasers (ECDLs) with 52 mW in total.

(c) In the cleanup region, B_{0-1}^C (690 nm) is from two sets of ILAs with 90 mW of power, A_{1-0}^C (637 nm) is from two sets of ILAs with 88 mW, and A_{1-2}^C (758 nm) or A_{0-1}^C (762 nm) is from a SolsTiS continuous-wave Ti:sapphire laser, with 93 mW and a 1 GHz EOM to address the spin-rotation states.

(d) In the detection region, B_{0-0}^D (635 nm) is from two ECDLs with 60 mW of power, A_{0-0}^D (695 nm) or A_{1-1}^D (693 nm) is from two ILAs with 96 mW of power.

The frequencies of all the transitions that we used are in Table VII. All frequencies are measured transversely to the molecular beam, with ≤ 10 MHz statistical uncertainties and ≤ 60 MHz systematic uncertainties from the wavemeter. The HFS in the ground states is clearly resolved in all spectra, while the HFS in the excited states is not resolved. Our measurements are consistent with previous work [57].

APPENDIX C: DETAILS OF MEASUREMENT STAGES

The general principle for designing measurement stages is to have at least as many independent equations as parameters, which includes the B -state predissociation probability. If the numbers of equations and parameters are equal, as in the cases of $B(v' = 0)$ and $B(v' = 1)$ using method I, we can directly express P_{pd} using the measured ratios. Other parameters will also be determined and analyzed, to serve as consistency checks. When there are more equations than parameters, we define a cost function to minimize the differences between the left- and right-hand sides of all equations (Appendix D). Here we present a detailed explanation of how the stages are used for predissociation probability measurements. We first discuss the simplest $B^2\Sigma^+(v' = 0)$ measurement, where the stages include the following:

Unperturbed. Only the $X(v'' = 0) \rightarrow B(v' = 0)$ detection lasers are turned on. This stage serves as molecule number calibration. By taking ratios of other stages to this stage, we can eliminate molecule number N from the expressions.

Cleanup. B_{0-1}^C vibrational repumpers are turned on. This stage helps to estimate the $X(v'' = 1)$ natural population.

X-A Cycling. A_{0-0}^I cycling lasers are turned on. This stage can be used to estimate the vibrational population distribution after X-A cycling, and measure the depletion efficiency.

X-A Cycling + Cleanup. A_{0-0}^I cycling lasers and B_{0-1}^C repumps are turned on. This stage helps to measure the repump efficiency, given the $X(v'' = 1)$ natural population.

X-B Cycling. B_{0-0}^I cycling lasers are turned on. This stage helps to measure the vibrational population distribution after X-B cycling.

X-B Cycling + Cleanup. B_{0-0}^I cycling lasers and B_{0-1}^C repumpers are turned on. Combined with previous stages, this helps to measure the $B^2\Sigma^+$ state predissociation probability.

To understand the stages better, let us take an example when N ground-state molecules interact with the $X(v'' = 0) \rightarrow A(v' = 0)$ laser. After optical cycling, the downstream ground-state population decreases to $d_A N$ (where $d_A < 1$ and is measurable simply by taking the ratios of signals). In this process, we describe the depletion efficiency as $1 - d_A$. We can also describe how d_A is distributed among the different vibrational levels of $X^2\Sigma^+$ using the known VBRs. For example, the population in $X(v'' = 1)$ is $N(1 - d_A)F_{A01}/\mathcal{F}_{A0} + n_1 N$, where F_{A01} , \mathcal{F}_{A0} , and n_1 represent the VBR for $A(v' = 0) \rightarrow X(v'' = 1)$, the sum of VBRs for $A(v' = 0) \rightarrow X(v'' = 1, 2, 3, \dots)$, and normalized $X(v'' = 1)$ natural population, because when a molecule is excited to $B(v' = 0)$ it eventually decays to a vibrational level or breaks apart. This process follows a discrete probability distribution based on the VBRs and P_{pd} . In the case discussed above, $(1 - d_A)N$ molecules leave $B(v' = 0)$, and, based on the law of large numbers, we expect the $X(v'' = 1)$ population to become $N(1 - d_A)F_{A01}/\mathcal{F}_{A0}$.

Note that our description relies on population transfer $(1 - d_A)$ rather than the number of scattered photons. In addition, the measurement protocol does not rely on the lasers having good overlap with the molecular beam or with each other, because as long as molecules share the same spatial and velocity distributions shot to shot, the parameters (e.g., cleanup efficiency) remain constant.

Here we briefly introduce the stages in method I of the $B^2\Sigma^+(v' = 1) P_{pd}$ measurement:

(1) *Unperturbed.* We always monitor the $X(v'' = 0)$ population, which serves as calibration.

(2) *Cleanup.* With an A_{0-1}^C laser, we pump the natural population in $X(v'' = 1)$ to $X(v'' = 0)$ to check cleanup efficiency.

(3) *State Prep.* With A_{1-0}^S laser, we pump the natural population in $X(v'' = 0)$ to $X(v'' = 1)$ to check state preparation efficiency. Only after efficiently pumping molecules to $X(v'' = 1)$ can we perform high-SNR optical cycling on $X(v'' = 1) \rightarrow B(v' = 1)$. Otherwise, the predissociation loss is too low to measure.

(4) *State Prep + Cleanup.* We first populate $X(v'' = 1)$ with an A_{1-0}^S laser, then move the $X(v'' = 1)$ population back to $X(v'' = 0)$. The signal size should be comparable to the unperturbed case. This step helps to measure κ , a , and n_1 , which are cleanup efficiency, state preparation efficiency, and $X(v'' = 1)$ natural population.

(5) *State Prep + X-B 1-1 Cycling.* With most molecules in the $X(v'' = 1)$ state, we can perform optical cycling via $B(v' = 1)$. We expect a signal increment compared to State Prep due to optical cycling and a redistribution of population based on VBR and P_{pd} .

(6) *State Prep + X-B 1-1 Cycling + Cleanup.* By cleaning up the population in $X(v'' = 1)$, we measure the molecules left in $X(v'' = 1)$ after optical cycling. Combined with previous stages, this provides five equations and five variables including P_{pd} .

Method II is designed as follows. We first perform state preparation to populate the $X(v'' = 1)$ state, similar to method I. By individually repumping the population that leaks to $X(v'' = 0)$ and $X(v'' = 2)$ we get a measure of unwanted loss. This also serves as a comparison of $A^2\Pi_{1/2}$ and $B^2\Sigma^+$ states in terms of the loss distribution. The ten stages are detailed in Table IV. The fact that method II accounts for losses to both $X(v'' = 0)$ and $X(v'' = 2)$ has advantages and disadvantages. On the one hand, method II provides an additional confidence check, with more equations than variables. Our approach to solving the overconstrained equation sets is in Appendix D. On the other hand, the method relies on detection using the $X(v'' = 1)$ state, which leads to lower signals and higher drift sensitivity than detecting on $X(v'' = 0)$. Hence the SNR for method II is not significantly higher than for method I.

Measuring the predissociation probability for $B^2\Sigma^+(v' = 2)$ and higher vibrational levels would require pumping the population to $X^2\Sigma^+(v'' = 2)$ and higher and performing optical cycling there, with repumping to recover the population, and monitoring unexplained loss. However, due to practical limitations in available space and number of lasers, as well as the increased complexity of the required stages, we did not pursue these measurements.

Table VIII contains stage details for the three types of measurement described above.

APPENDIX D: BOOTSTRAP METHOD USED IN THE PREDISSOCIATION DATA ANALYSIS

Bootstrapping is a statistical technique that involves generating multiple samples from a data set by sampling with

TABLE VIII. Complete stage information for the $B^2\Sigma^+$ state predissociation measurement (also summarized in Tables II-IV). For $B(v' = 0)$ we use five variables: $n_1, \kappa, F_{B0a}, d_A,$ and $d_B,$ representing $X(v'' = 1)$ natural population, cleanup efficiency of laser $B_{-0}^C,$ the $B(v' = 0)$ state predissociation probability, depletion efficiency of laser $A_{-0}^I,$ and depletion efficiency of laser $B_{-0}^I.$ For $B(v' = 1)$ method I, the five variables used are $a, n_1, \kappa, F_{B1a},$ and $d_B,$ representing state preparation (from $X(v'' = 0)$ to $X(v'' = 1)$) efficiency, $X(v'' = 1)$ natural population, cleanup efficiency of laser $B_{-1}^C,$ the seven variables are $a, n_1, \kappa, \kappa_2, F_{B1a}, d_A,$ and $d_B,$ representing state preparation (from $X(v'' = 0)$ to $X(v'' = 1)$) efficiency, cleanup efficiency of laser $A_{-1}^C,$ cleanup efficiency of laser $A_{-1}^C,$ the $B(v' = 1)$ state predissociation probability, depletion efficiency of laser $A_{-1}^I,$ and depletion efficiency of laser $B_{-1}^I.$ We denote the VBR normalization factors as $\mathcal{F}_{A_0} \equiv \sum_{i \neq 0} F_{A0i}, \mathcal{F}_{A_1} \equiv \sum_{i \neq 1} F_{A0i}, \mathcal{F}_{A_2} \equiv \sum_{i \neq 0} F_{A1i}, \mathcal{F}_{A_3} \equiv \sum_{i \neq 1} F_{A1i}, \mathcal{F}_{B_0} \equiv F_{B0a} + \sum_{i \neq 0} F_{B0i}, \mathcal{F}_{B_1} \equiv F_{B0a} + \sum_{i \neq 0} F_{B0i},$ and $\mathcal{F}_{B_2} \equiv F_{B1a} + \sum_{i \neq 1} F_{B1i}.$

Purpose	Laser configuration	$X^2\Sigma^+(v'' = 0)$ state population normalized	$X^2\Sigma^+(v'' = 1)$ state population normalized	$X^2\Sigma^+(v'' = 2)$ state population normalized
Unperturbed		$v' = 0$ experiment		
Cleanup	B_{0-1}^C	1	n_1	≈ 0
X-A Cycling	A_{0-0}^I	$1 + n_1\kappa F_{B00}/\mathcal{F}_{B_0}$	$n_1(1 - \kappa)$	$n_1\kappa F_{B02}/\mathcal{F}_{B_0}$
X-A Cycling + Cleanup	$A_{0-0}^I + B_{0-1}^C$	d_A	$(1 - d_A)F_{A01}/\mathcal{F}_{A_0} + n_1$	$(1 - d_A)F_{A02}/\mathcal{F}_{A_0}$
X-B Cycling	B_{0-0}^I	$d_A + [(1 - d_A)F_{A01}/\mathcal{F}_{A_0} + n_1]\kappa F_{B00}/\mathcal{F}_{B_0}$	$[(1 - d_A)F_{A01}/\mathcal{F}_{A_0} + n_1](1 - \kappa)$	$[(1 - d_A)F_{A01}/\mathcal{F}_{A_0} + n_1]\kappa F_{B02}/\mathcal{F}_{B_0}$ $+ (1 - d_A)F_{A02}/\mathcal{F}_{A_0}$
X-B Cycling + Cleanup	$B_{0-0}^I + B_{0-1}^C$	d_B	$(1 - d_B)F_{B01}/\mathcal{F}_{B_1} + n_1$	$(1 - d_B)F_{B02}/\mathcal{F}_{B_1}$
Unperturbed		$v' = 1$ experiment, method I		
State Prep	A_{1-0}^S	1	n_1	≈ 0
Cleanup	A_{0-1}^C	$1 - a$	$n_1 + aF_{A11}/\mathcal{F}_{A_2}$	$aF_{A12}/\mathcal{F}_{A_2}$
State Prep + Cleanup	$A_{1-0}^S + A_{0-1}^C$	$1 + n_1\kappa F_{A00}/\mathcal{F}_{A_1}$	$n_1\kappa F_{A02}/\mathcal{F}_{A_1}$	$n_1\kappa F_{A02}/\mathcal{F}_{A_1}$
State Prep + X-B 1-1 Cycling	$A_{1-0}^S + B_{1-1}^I$	$1 - a + (n_1 + aF_{A11}/\mathcal{F}_{A_2})\kappa F_{A00}/\mathcal{F}_{A_1}$	$(n_1 + aF_{A11}/\mathcal{F}_{A_2})(1 - \kappa)$	$aF_{A12}/\mathcal{F}_{A_2} + (n_1 + aF_{A11}/\mathcal{F}_{A_2})\kappa F_{A02}/\mathcal{F}_{A_1}$
State Prep + X-B 1-1 Cycling + Cleanup	$A_{1-0}^S + B_{1-1}^I + A_{0-1}^C$	$1 - a + (n_1 + aF_{A11}/\mathcal{F}_{A_2})d_B F_{B10}/\mathcal{F}_{B_2}$	$(n_1 + aF_{A11}/\mathcal{F}_{A_2})(1 - d_B)$	$aF_{A12}/\mathcal{F}_{A_2} + (n_1 + aF_{A11}/\mathcal{F}_{A_2})d_B F_{B12}/\mathcal{F}_{B_2}$
		$1 - a + (n_1 + aF_{A11}/\mathcal{F}_{A_2})(d_B F_{B10}/\mathcal{F}_{B_2} + (1 - d_B)\kappa F_{A00}/\mathcal{F}_{A_1})$	$(n_1 + aF_{A11}/\mathcal{F}_{A_2})(1 - \kappa)(1 - d_B)$	$aF_{A12}/\mathcal{F}_{A_2} + (n_1 + aF_{A11}/\mathcal{F}_{A_2})(d_B F_{B12}/\mathcal{F}_{B_2} + (1 - d_B)\kappa F_{A02}/\mathcal{F}_{A_1})$

TABLE VIII. (Continued.)

Purpose	Laser configuration	$X^2\Sigma^+(v''=0)$ state population normalized	$v' = 1$ experiment, method II	$X^2\Sigma^+(v''=1)$ state population normalized	$X^2\Sigma^+(v''=2)$ state population normalized
State Prep + Cleanup v0	$A_{1-0}^S + A_{1-0}^C$	$(1-a)(1-\kappa_1)$	$n_1 + (a + \kappa_1 - a\kappa_1)F_{A11}/F_{A_2}$	$(a + \kappa_1 - a\kappa_1)F_{A12}/F_{A_2}$	
Unperturbed			n_1	≈ 0	
State Prep	A_{1-0}^S	$1-a$	$n_1 + aF_{A11}/F_{A_2} \equiv \mathcal{Z}$	aF_{A12}/F_{A_2}	
Cleanup v0	A_{1-0}^C	$1-\kappa_1$	$n_1 + \kappa_1 F_{A11}/F_{A_2}$	$\kappa_1 F_{A12}/F_{A_2}$	
State Prep + X-A 1-1 Cycling	$A_{1-0}^S + A_{1-1}^C$	$1-a + \mathcal{Z}d_A F_{A10}/F_{A_3}$	$\mathcal{Z}(1-d_A)$	$aF_{A12}/F_{A_2} + \mathcal{Z}d_A F_{A12}/F_{A_3}$	
State Prep + X-A 1-1 Cycling + Cleanup v0	$A_{1-0}^S + A_{1-1}^C + A_{1-0}^C$	$(1-a + \mathcal{Z}d_A F_{A10}/F_{A_3})(1-\kappa_1)$	$\mathcal{Z}(1-d_A) + (1-a + \mathcal{Z}d_A F_{A10}/F_{A_3})\kappa_1 F_{A11}/F_{A_2}$	$aF_{A12}/F_{A_2} + \mathcal{Z}d_A F_{A10}/F_{A_3} + (1-a + \mathcal{Z}d_A F_{A10}/F_{A_3})\kappa_1 F_{A12}/F_{A_2}$	
State Prep + X-A 1-1 Cycling + Cleanup v2	$A_{1-0}^S + A_{1-1}^C + A_{1-2}^C$	$1-a + \mathcal{Z}d_A F_{A10}/F_{A_3} + (aF_{A12}/F_{A_2} + \mathcal{Z}d_A F_{A12}/F_{A_3})\kappa_2 F_{A10}/F_{A_4}$	$\mathcal{Z}(1-d_A) + (aF_{A12}/F_{A_2} + \mathcal{Z}d_A F_{A12}/F_{A_3})\kappa_2 F_{A11}/F_{A_4}$	$aF_{A12}/F_{A_2} + \mathcal{Z}d_A F_{B12}/F_{B_2}$	
State Prep + X-B 1-1 Cycling	$A_{1-0}^S + B_{1-1}^C$	$1-a + \mathcal{Z}d_B F_{B10}/F_{B_2}$	$\mathcal{Z}(1-d_B)$	$aF_{A12}/F_{A_2} + \mathcal{Z}d_B F_{B12}/F_{B_2}$	
State Prep + X-B 1-1 Cycling + Cleanup v0	$A_{1-0}^S + B_{1-1}^C + A_{1-0}^C$	$(1-a + \mathcal{Z}d_B F_{B10}/F_{B_2})(1-\kappa_1)$	$\mathcal{Z}(1-d_B) + (1-a + \mathcal{Z}d_B F_{B10}/F_{B_2})\kappa_1 F_{A11}/F_{A_2}$	$aF_{A12}/F_{A_2} + \mathcal{Z}d_B F_{B10}/F_{B_2} + (1-a + \mathcal{Z}d_B F_{B10}/F_{B_2})\kappa_1 F_{A12}/F_{A_2}$	
State Prep + X-B 1-1 Cycling + Cleanup v2	$A_{1-0}^S + B_{1-1}^C + A_{1-2}^C$	$1-a + \mathcal{Z}d_B F_{B10}/F_{B_2} + (aF_{A12}/F_{A_2} + \mathcal{Z}d_B F_{B12}/F_{B_2})\kappa_2 F_{A10}/F_{A_4}$	$\mathcal{Z}(1-d_B) + (aF_{A12}/F_{A_2} + \mathcal{Z}d_B F_{B12}/F_{B_2})\kappa_2 F_{A11}/F_{A_4}$	$(aF_{A12}/F_{A_2} + \mathcal{Z}d_B F_{B12}/F_{B_2})(1-\kappa_2)$	

replacement [45]. It is a useful tool for constructing confidence intervals for a population parameter—in this case, the expectation values of predissociation probabilities.

A key benefit of bootstrapping is that it allows one to make inferences about a population based on a sample, without making any assumptions about the underlying distribution of the population. Given the complexity of the functional form of predissociation probability with respect to experimentally measured ratios, utilizing a bootstrap method helps to avoid assuming a normal distribution when determining the confidence interval of predissociation probabilities.

One way to use such a method on a set of data d with size n is to use the array of d data points to generate n “bootstrapped” samples by sampling with replacement. We can then compute a statistic of interest, such as the mean, from the n bootstrapped samples, and save it to a new array. We repeatedly generate n bootstrapped samples, calculate the mean, and save it to the storage array. The resulting distribution of the statistic can then be used to make inferences about the population.

Let us consider the $B(v' = 0)$ predissociation probability as an example. The experimental procedure to acquire ratios is shown in Fig. 2 and explained in Sec. VD. All the ratios (r_1, r_2, r_3, r_4, r_5) are expressed using the variables in Table II, including $n_1, \kappa, F_{B0a}, d_A$, and d_B . Five equations can be explicitly written as

$$\begin{aligned}
 r_1 &= 1 + n_1 \kappa F_{B00}/F_{B_0}, \\
 r_2 &= d_A, \\
 r_3 &= d_A + [(1-d_A)F_{A01}/F_{A_0} + n_1] \kappa F_{B00}/F_{B_0}, \\
 r_4 &= d_B, \\
 r_5 &= d_B + [(1-d_B)F_{B01}/F_{B_1} + n_1] \kappa F_{B00}/F_{B_0}.
 \end{aligned}
 \tag{D1}$$

By solving these five equations for five variables, we can express F_{B0a} as a function of r_i ($i \in \{1, 2, 3, 4, 5\}$) with known VBRs. Therefore, we obtain a function f_{B0a} that takes in r_i ($i \in \{1, 2, 3, 4, 5\}$) and outputs predissociation probability F_{B0a} . Here we describe the procedure of performing bootstrap analysis on the data, where the data consist of $n \approx 200$ sets of ratios $\{r_1, r_2, r_3, r_4, r_5\}$, with r_i ($i \in \{1, 2, 3, 4, 5\}$) being an array of length n :

(1) Randomly sample n elements from the original r_1 array with replacement; i.e., elements from the original r_1 can appear more than once in the new array r_1^{bt} . This step mimics the situation where the same measurement is performed again. We carry out independent random sampling with replacement for r_2, r_3, r_4 , and r_5 as well, and obtain r_i^{bt} ($i \in \{1, 2, 3, 4, 5\}$) arrays.

(2) Calculate the mean of the newly generated r_i^{bt} arrays individually, which can be denoted as $\overline{r_i^{\text{bt}}}$. We can feed these $\overline{r_i^{\text{bt}}}$ s to the function f_{B0a} and store the output in an array F .

(3) Repeat steps 1 and 2 for $\sim 10^6$ times, until the statistical properties such as mean and standard deviation of the normalized distribution of array F converge.

(4) Analyze the distribution of F . For the expectation value, we use the mean of array F . To determine the 95% confidence interval, we take the 2.5% quantile from the distribution of F as the lower bound, and the 97.5% quantile as the upper bound.

The data analysis for $B(v' = 1)$ method I is almost identical to that for $B(v' = 0)$. The bootstrap procedures are the same, and the analysis code can be found online [59].

The data analysis for $B(v' = 1)$ method II is slightly different from the previous two cases. We no longer have a deterministic function of F_{B1a} because there are nine equations with seven variables. To solve this overconstrained system, we perform a least-squares fit. We write down the nine equations with all the terms on the right-hand side and zeros on the left-hand side. Then we define the cost function as the sum of squares of all the right-hand sides of the equations, and use the Levenberg-Marquardt algorithm to search for the local minimum with a reasonable initial guess.

APPENDIX E: THEORETICAL DETAILS

The following three-state Hamiltonian (for the $X^2\Sigma^+$, $B^2\Sigma^+$, and $D^2\Sigma^+$ electronic states) is diagonalized to obtain wavefunctions, FCFs, and predissociation estimates:

$$\sum_j^3 H_j = \sum_l \frac{(\hat{p}^l + A_{ij}^l(r))^2}{2\mu} \phi_j(r) + V_j(r) \phi_j(r). \quad (\text{E1})$$

The first term is the kinetic energy operator, in which \hat{p} is the standard momentum operator, expressed on a grid via the Colbert-Miller derivative. We represent the momentum operator in position space so that we can incorporate the nonadiabatic coupling term directly. This term is computed in the position representation, $A_{ij}(r) = \langle \Psi_i | \hat{p} | \Psi_j \rangle$. We obtain $\langle \Psi_i | \frac{\partial}{\partial r} | \Psi_j \rangle$ from a $dr = 0.001a_0$ potential energy surface scan via MOLPRO electronic structure calculations, and interpolate this onto a spline to represent $A_{ij}(r)$. The reduced mass of CaH is μ . Finally, $V(r)$ is obtained from the $dr = 0.001a_0$ scan via the MRCI+Q Davidson energies and interpolated onto a spline before being incorporated into the Hamiltonian.

At $r_0 = 8$ a.u., an optical potential of the form $-iV(r - r_0)^2/w^2$ is added only to the $X^2\Sigma^+$ state's $V(r)$ at

TABLE IX. Calculated and measured values of FCFs for CaH. We show experimental FCFs [19] for comparison. A' is the same active space as the $B^2\Sigma^+$ state in this work, shifting the potential to the left by $0.0375a_0$.

Transition	Vibrational quanta (v'')	FCF calculated ($f_{0v''}$)	FCF measured ($f_{0v''}$)
$A' \rightarrow X$	0	0.9568	0.9572(43)
	1	0.0401	0.0386(32)
	2	2.9×10^{-3}	$4.2(3.2) \times 10^{-3}$
	3	2.5×10^{-4}	

the PES asymptote with each grid point to simulate the continuum and create a flux equation. Specifically, the optical absorbing potential must have a width w and depth V which guarantees complete wave-packet absorption and ensures the potential is smooth so that hardly any reflection takes place before the wave packet enters the potential [44]. The absorber width is chosen to be $w = 8a_0$, much larger than the typical de Broglie wavelength of $\sim 0.2a_0$. We choose a depth as the typical energy of the wave packet, or 0.2 a.u. ($4.4 \times 10^4 \text{ cm}^{-1}$). The Hamiltonian is then diagonalized. The optical potential enforces imaginary eigenvalues that are directly related to nonradiative loss rates, which are then compared to the radiative rates calculated from the MRCI-computed transition dipole moments to obtain a predissociation probability.

For spin-orbit coupling, the active space for $X^2\Sigma^+$, $A^2\Pi_{1/2}$, and $B^2\Sigma^+$ states must be the same; therefore, a compromise is chosen to optimize the $X^2\Sigma^+$ and $B^2\Sigma^+$ FCFs over the $A^2\Pi_{1/2}$. Interestingly, we note that using our basis set and active space but shifting the $A^2\Pi_{1/2}$ potential energy surface can produce FCFs that are equivalent to experimentally measured values, as shown in Table IX. This is because static electron correlation has converged, but important dynamic correlation is missing. This depends on the original orbital active space from CASSCF which then affects the MRCI equilibrium bond length.

-
- [1] H. J. Metcalf and P. van der Straten, *Laser Cooling and Trapping* (Springer, New York, 1999)
- [2] A. H. Myerson, D. J. Szwer, S. C. Webster, D. T. C. Allcock, M. J. Curtis, G. Imreh, J. A. Sherman, D. N. Stacey, A. M. Steane, and D. M. Lucas, High-fidelity readout of trapped-ion qubits, *Phys. Rev. Lett.* **100**, 200502 (2008).
- [3] R. Blatt and C. F. Roos, Quantum simulations with trapped ions, *Nat. Phys.* **8**, 277 (2012).
- [4] S. Shuman, J. Barry, and D. DeMille, Laser cooling of a diatomic molecule, *Nature (London)* **467**, 820 (2010).
- [5] S. Truppe, H. J. Williams, M. Hambach, L. Caldwell, N. J. Fitch, E. A. Hinds, B. E. Sauer, and M. R. Tarbutt, Molecules cooled below the Doppler limit, *Nat. Phys.* **13**, 1173 (2017).
- [6] L. Anderegg, B. L. Augenbraun, Y. Bao, S. Burchesky, L. W. Cheuk, W. Ketterle, and J. M. Doyle, Laser cooling of optically trapped molecules, *Nat. Phys.* **14**, 890 (2018).
- [7] L. Anderegg, L. W. Cheuk, Y. Bao, S. Burchesky, W. Ketterle, K.-K. Ni, and J. M. Doyle, An optical tweezer array of ultracold molecules, *Science* **365**, 1156 (2019).
- [8] Y. Wu, J. J. Burau, K. Mehling, J. Ye, and S. Ding, High phase-space density of laser-cooled molecules in an optical lattice, *Phys. Rev. Lett.* **127**, 263201 (2021).
- [9] N. B. Vilas, C. Hallas, L. Anderegg, P. Robichaud, A. Winnicki, D. Mitra, and J. M. Doyle, Magneto-optical trapping and sub-Doppler cooling of a polyatomic molecule, *Nature (London)* **606**, 70 (2022).
- [10] D. Mitra, N. B. Vilas, C. Hallas, L. Anderegg, B. L. Augenbraun, L. Baum, C. Miller, S. Raval, and J. M. Doyle, Direct laser cooling of a symmetric top molecule, *Science* **369**, 1366 (2020).
- [11] B. Hemmerling, E. Chae, A. Ravi, L. Anderegg, G. K. Drayna, N. R. Hutzler, A. L. Collopy, J. Ye, W. Ketterle, and J. M. Doyle, Laser slowing of CaF molecules to near the capture

- velocity of a molecular MOT, *J. Phys. B: At. Mol. Opt. Phys.* **49**, 174001 (2016).
- [12] H. J. Williams, S. Truppe, M. Hambach, L. Caldwell, N. J. Fitch, E. A. Hinds, B. E. Sauer, and M. R. Tarbutt, Characteristics of a magneto-optical trap of molecules, *New J. Phys.* **19**, 113035 (2017).
- [13] N. R. Hutzler, H.-I. Lu, and J. M. Doyle, The buffer gas beam: An intense, cold, and slow source for atoms and molecules, *Chem. Rev.* **112**, 4803 (2012).
- [14] P. Aggarwal, Y. Yin, K. Esajas, H. L. Bethlem, A. Boeschoten, A. Borschevsky, S. Hoekstra, K. Jungmann, V. R. Marshall, T. B. Meijknecht, M. C. Mooij, R. G. E. Timmermans, A. Touwen, W. Ubachs, and L. Willmann (NL-*e*EDM Collaboration), Deceleration and trapping of SrF molecules, *Phys. Rev. Lett.* **127**, 173201 (2021).
- [15] M. Zeppenfeld, B. G. U. Englert, R. Glöckner, A. Prehn, M. Mielenz, C. Sommer, L. D. van Buuren, M. Motsch, and G. Rempe, Sisyphus cooling of electrically trapped polyatomic molecules, *Nature (London)* **491**, 570 (2012).
- [16] X. Wu, T. Gantner, M. Koller, M. Zeppenfeld, S. Chervakov, and G. Rempe, A cryofuge for cold-collision experiments with slow polar molecules, *Science* **358**, 645 (2017).
- [17] B. L. Augenbraun, A. Frenett, H. Sawaoka, C. Hallas, N. B. Vilas, A. Nasir, Z. D. Lasner, and J. M. Doyle, Zeeman-Sisyphus deceleration of molecular beams, *Phys. Rev. Lett.* **127**, 263002 (2021).
- [18] M. D. DiRosa, Laser-cooling molecules: Concept, candidates, and supporting hyperfine-resolved measurements of rotational lines in the *A-X*(0, 0) band of CaH, *Eur. Phys. J. D* **31**, 395 (2004).
- [19] S. F. Vázquez-Carson, Q. Sun, J. Dai, D. Mitra, and T. Zelevinsky, Direct laser cooling of calcium monohydride molecules, *New J. Phys.* **24**, 083006 (2022).
- [20] Y. Gao and T. Gao, Laser cooling of the alkaline-earth-metal monohydrides: Insights from an *ab initio* theory study, *Phys. Rev. A* **90**, 052506 (2014).
- [21] G. Herzberg, *Molecular Spectra and Molecular Structure, I. Spectra of Diatomic Molecules* (D. Van Nostrand Company, Princeton, NJ, 1950).
- [22] W. Demtröder, *Molecular Physics* (Wiley-VCH Verlag, Weinheim, Germany, 2005).
- [23] J. von Neumann and E. Wigner, Über merkwürdige diskrete eigenwerte. Über das verhalten von eigenwerten bei adiabatischen prozessen, *Phys. Z.* **30**, 467 (1929).
- [24] E. Teller, The crossing of potential surfaces, *J. Phys. Chem.* **41**, 109 (1937).
- [25] C. A. Mead, The “noncrossing” rule for electronic potential energy surfaces: The role of time-reversal invariance, *J. Chem. Phys.* **70**, 2276 (1979).
- [26] I. C. Lane, Production of ultracold hydrogen and deuterium via Doppler-cooled Feshbach molecules, *Phys. Rev. A* **92**, 022511 (2015).
- [27] P. K. H.-J. Werner *et al.*, MOLPRO, version 2022.3, a package of *ab initio* programs, <https://www.molpro.net> (2022).
- [28] H.-J. Werner, P. J. Knowles, G. Knizia, F. R. Manby, and M. Schütz, MOLPRO: A general-purpose quantum chemistry program package, *WIREs Comput. Mol. Sci.* **2**, 242 (2012).
- [29] H.-J. Werner, P. J. Knowles, F. R. Manby, J. A. Black, K. Doll, A. Heßelmann, D. Kats, A. Köhn, T. Korona, D. A. Kreplin *et al.*, The MOLPRO quantum chemistry package, *J. Chem. Phys.* **152**, 144107 (2020).
- [30] A. Shayesteh, S. F. Alavi, M. Rahman, and E. Gharib-Nezhad, *Ab initio* transition dipole moments and potential energy curves for the low-lying electronic states of CaH, *Chem. Phys. Lett.* **667**, 345 (2017).
- [31] J. Koput and K. A. Peterson, *Ab initio* potential energy surface and vibrational-rotational energy levels of $X^2\Sigma^+$ CaOH, *J. Phys. Chem. A* **106**, 9595 (2002).
- [32] T. H. Dunning, Jr., Gaussian basis sets for use in correlated molecular calculations. I. The atoms boron through neon and hydrogen, *J. Chem. Phys.* **90**, 1007 (1989).
- [33] P. J. Knowles and H.-J. Werner, An efficient second-order MC SCF method for long configuration expansions, *Chem. Phys. Lett.* **115**, 259 (1985).
- [34] H.-J. Werner and P. J. Knowles, An efficient internally contracted multiconfiguration-reference configuration interaction method, *J. Chem. Phys.* **89**, 5803 (1988).
- [35] P. J. Knowles and H.-J. Werner, Internally contracted multiconfiguration-reference configuration interaction calculations for excited states, *Theor. Chim. Acta* **84**, 95 (1992).
- [36] K. Shamasundar, G. Knizia, and H.-J. Werner, A new internally contracted multi-reference configuration interaction method, *J. Chem. Phys.* **135**, 054101 (2011).
- [37] A. Berning, M. Schweizer, H.-J. Werner, P. J. Knowles, and P. Palmieri, Spin-orbit matrix elements for internally contracted multireference configuration interaction wavefunctions, *Mol. Phys.* **98**, 1823 (2000).
- [38] D. T. Colbert and W. H. Miller, A novel discrete variable representation for quantum mechanical reactive scattering via the S-matrix Kohn method, *J. Chem. Phys.* **96**, 1982 (1992).
- [39] T. Busch, A. D. Esposti, and H.-J. Werner, Analytical energy gradients for multiconfiguration self-consistent field wave functions with frozen core orbitals, *J. Chem. Phys.* **94**, 6708 (1991).
- [40] R. Baer, *Electron Density Functional Theory* (Fritz Haber Center for Molecular Dynamics, The Hebrew University of Jerusalem, Jerusalem, Israel, 2016).
- [41] D. Neuhauser and M. Baer, The application of wave packets to reactive atom-diatom systems: A new approach, *J. Chem. Phys.* **91**, 4651 (1989).
- [42] D. Neuhauser, State-to-state reactive scattering amplitudes from single-arrangement propagation with absorbing potentials, *J. Chem. Phys.* **93**, 7836 (1990).
- [43] D. Neuhauser, Molecular scattering: Very-short-range imaginary potentials, absorbing-potentials, and flux-amplitude expressions, *J. Chem. Phys.* **103**, 8513 (1995).
- [44] D. Neuhauser and M. Baer, The time-dependent Schrödinger equation: Application of absorbing boundary conditions, *J. Chem. Phys.* **90**, 4351 (1989).
- [45] B. Efron, Bootstrap methods: Another look at the jackknife, *Ann. Stat.* **7**, 1 (1979).
- [46] B. Efron and R. J. Tibshirani, *An Introduction to the Bootstrap*, Monographs on Statistics and Applied Probability No. 57 (Chapman & Hall/CRC, Boca Raton, FL, 1993).
- [47] A. C. Davison and D. V. Hinkley, *Bootstrap Methods and their Application*, Cambridge Series in Statistical and Probabilistic Mathematics (Cambridge University Press, Cambridge, UK, 1997).

- [48] M. Ramanaiah and S. Lakshman, True potential energy curves and Franck-Condon factors of a few alkaline earth hydrides, *Physica C* **113**, 263 (1982).
- [49] A. Kawasaki, Magic wavelength for the hydrogen $1S$ - $2S$ transition, *Phys. Rev. A* **92**, 042507 (2015).
- [50] B. H. McGuyer, M. McDonald, G. Z. Iwata, M. G. Tarallo, A. T. Grier, F. Apfelbeck, and T. Zelevinsky, High-precision spectroscopy of ultracold molecules in an optical lattice, *New J. Phys.* **17**, 055004 (2015).
- [51] M. McDonald, B. H. McGuyer, F. Apfelbeck, C.-H. Lee, I. Majewska, R. Moszynski, and T. Zelevinsky, Photodissociation of ultracold diatomic strontium molecules with quantum state control, *Nature (London)* **535**, 122 (2016).
- [52] N. V. Vitanov, A. A. Rangelov, B. W. Shore, and K. Bergmann, Stimulated Raman adiabatic passage in physics, chemistry, and beyond, *Rev. Mod. Phys.* **89**, 015006 (2017).
- [53] S. A. Moses, J. P. Covey, M. T. Miecikowski, D. S. Jin, and J. Ye, New frontiers for quantum gases of polar molecules, *Nat. Phys.* **13**, 13 (2017).
- [54] A. Vardi, M. Shapiro, and K. Bergmann, Complete population transfer to and from a continuum and the radiative association of cold Na atoms to produce translationally cold Na_2 molecules in specific vib-rotational states, *Opt. Express* **4**, 91 (1999).
- [55] A. A. Rangelov, N. V. Vitanov, and E. Arimondo, Stimulated Raman adiabatic passage into continuum, *Phys. Rev. A* **76**, 043414 (2007).
- [56] V. Barbé, A. Ciamei, B. Pasquiou, L. Reichsöllner, F. Schreck, P. S. Żuchowski, and J. M. Hutson, Observation of Feshbach resonances between alkali and closed-shell atoms, *Nat. Phys.* **14**, 881 (2018).
- [57] A. Shayesteh, R. S. Ram, and P. F. Bernath, Fourier transform emission spectra of the $A^2\Pi-X^2\Sigma^+$ and $B^2\Sigma^+-X^2\Sigma^+$ band systems of CaH, *J. Mol. Spectrosc.* **288**, 46 (2013).
- [58] E. B. Norrgard, Magneto-optical trapping of diatomic molecules, Ph.D. thesis, Yale University, 2016.
- [59] github.com/QiSun97/CaH_Predissociation/bootstrapping_v6_final_github.ipynb.